



Supplementary Materials for

Flavivirus NS1 crystal structures reveal a surface for membrane association and regions of interaction with the immune system

David L. Akey, W. Clay Brown, Somnath Dutta, Jamie Konwerski, Joyce Jose, Thomas J. Jurkiw, James DelProposto, Craig M. Ogata, Georgios Skiniotis, Richard J. Kuhn & Janet L. Smith

correspondence to: JanetSmith@umich.edu

This PDF file includes:

Materials and Methods
Figs. S1 to S6
Tables S1 to S2
References

Materials and Methods

Construction, cloning and expression evaluation

The construction of the West Nile virus (WNV; NY99) and dengue virus type 2 (DEN2; 16681) NS1 coding sequences, production of recombinant baculovirus and small-scale expression evaluation were carried out as previously described (27).

Lysis buffer screening

High-five and Sf9 cells at a density of 2×10^6 cells per mL were infected with baculovirus encoding the NS1 sequence fused with a secretion signal sequence (Ac-gp64 for WNV NS1, Op-gp64 for DEN2 NS1), followed by a His tag (27). After 72 hours, cells were transferred to a 24-well block. Cell pellets were resuspended and then sonicated 5 sec. The contents of each well were transferred to 1.7 mL microfuge tubes and centrifuged 10 min at 20,000 x g. The small-scale, high-throughput purification was then completed as previously described (27).

Large-scale production and purification of NS1 protein

Cell pellets (High Five for WNV NS1, Sf9 for DEN2 NS1) from 1 L NS1 infection cultures were resuspended at 4 mL/g with 50 mM Tris (pH8.5), 50 mM $(\text{NH}_4)_2\text{SO}_4$, 10% glycerol, 0.5% triton, and sonicated on ice 3 x 30 sec at 50% power. The lysate was cleared by centrifugation and the supernatant was diluted by 50% with buffer. Protein was batch bound to nickel resin for four hours. The slurry was poured into a column and the flow-through buffer was collected. The resin was washed with 50 volumes of buffer, and the protein was eluted in 10-15 volumes of buffer with 200 mM imidazole. Detergent was absent from the buffers in subsequent steps. The eluate was dialyzed, concentrated and further purified by gel filtration using a Superose S200 column. An alternative purification was carried out in which the wash and elution buffers for the metal-affinity chromatography step did not contain detergent and the dialysis step was omitted.

Crystallization

All crystals were grown by vapor diffusion at 4°C. WNV NS1 crystal form 1 grew by equilibrating ~7 mg/mL protein against a reservoir solution containing 20% – 25% PEG 3000 or PEG 3350, 5% glycerol, and 150 – 300 mM sodium citrate pH 5.5. Crystals formed in two weeks, but often were allowed to continue growing for up to six months before harvesting and data collection. Crystal form 2 grew in similar conditions, but over a pH range of 5.5 – 7.5. The data reported here were collected from a form 2 crystal grown with 25% PEG 3350, 250 mM sodium citrate pH 5.5. DEN2 NS1 crystals grew by equilibrating ~10 mg/mL protein against a reservoir solution containing 21% PEG 3350 and 250 mM ammonium formate pH 6.6. Crystals were harvested without additional cryoprotection and flash-cooled in liquid nitrogen.

Structure determination

The WNV NS1 structure in crystal form 1 was solved by native sulfur SAD phasing. Data were collected at GM/CA beamline 23-ID-D at the Advanced Photon Source at 7.1 keV using a 100-mm helium box to reduce air absorption. Complete data were collected from each crystal using 0.5° oscillations in inverse beam mode (90° of data in 5° wedges that were interleaved with 5° wedges of the Friedel-related 90° of data). Data (up to 3.0 Å maximum usable resolution) were integrated and scaled using XDS (28) (Table S1). Complete data sets from eighteen crystals

were scaled and combined using XSCALE for a final data multiplicity of 200 (anomalous multiplicity of 100 between 50 and 3 Å). A cut-off of ~0.8 in the CC* statistic (29, 30) was used to define d_{\min} for the merged data in this and all subsequent datasets. Anomalous signal was estimated to extend to ~5.4 Å. Data to 5.2 Å were used with SHELX (31) to find sulfur sites, including what were later determined to be all 12 cysteine disulfides and 8 of 10 methionines. Two-fold noncrystallographic symmetry (NCS) was identified by visual inspection of the sites, and the NCS operator was calculated using LSQKAB (32). Phases to 4.5 Å were calculated using SHELX, and these phases were extended and modified by DM (32) to 3.0 Å using the two-fold NCS operator and solvent flattening (75% solvent content). The resultant maps were readily interpretable (Fig. S2A), and an ~75% complete preliminary model was auto-built using Buccaneer (33). Disulfide and methionine sites were confirmed by inspection of the anomalous difference map, which in conjunction with the high occurrence of tryptophan, allowed us to build the chain trace and determine the correct register with a high degree of confidence. Model building was carried out using Coot (34) and refinement with Refmac (35) and Phenix (36). Native data to 2.6 Å were collected at 12 keV from a crystal grown using vapor diffusion under Al's oil (Hampton Research) (Table S1). Detergent molecule fragments (Triton X-100) were fit to residual density after all parts of the polypeptide had been assigned, by considering all components of the crystallization and purification solutions. The structure of WNV NS1 in crystal form 1 is complete with the exception of residues 108-128 (chain A) and 109-129 (chain B) and contains 5 of 6 identified glycosylation sites and several residues from N-terminal His₆ tags and linkers (11 in chain A and 21 in chain B). The WNV NS1 dimer structure was used with the molecular replacement program MOLREP (32) to solve structures of WNV NS1 in crystal form 2 (three dimers per asymmetric unit, forming three similar hexamers at crystallographic threefold axes) and DEN2 NS1 (one dimer per asymmetric unit, forming a hexamer at a crystallographic threefold axis). Both of these crystal forms were twinned. The structure of WNV NS1 in crystal form 2 has identical completeness in each of the six subunits in asymmetric unit, including all residues except 110-124. The DEN2 NS1 structure lacks residues 8-10, 108-128, 159-165 and 350-352 in chain A, and residues 107-130, 162-163 and 350-352 in chain B. The structures were validated by MolProbity (37). The dimer interface buries 2700 Å² of surface area per monomer, as analyzed by PISA (38). The β -roll accounts for 70% of the buried surface area.

Liposome preparation and NS1 interaction

Lipid solutions were made by dissolving cholesterol (CHOL) (Sigma) and 1, 2-dipalmitoyl-*sn*-glycero-3-phosphocholine (PC) in chloroform at ratios of 1:9 CHOL:PC. Portions of each solution were placed in glass tubes and dried under a stream of nitrogen. Liposomes were produced by adding 400 μ L of buffer (50 mM Bis-Tris pH 5.5, 50 mM (NH₄)₂SO₄, 10 % glycerol) to the dried lipids and then sonicating in a bath at 37 °C for approximately 5 min. Following removal of the N-terminal His₆-Mocr tag (27) with TEV protease, a 50 μ L sample of approximately 10 mg/mL NS1 protein was mixed with 150 μ L of the liposome solution in 1.5 mL tubes followed by 2 hr incubation at 37 °C and 30 min centrifugation at 13,000 RPM. The supernatant was removed and the soluble fraction and pellet were treated separately for electron microscopy. The methyltransferase MycE (39), which does not interact with membranes, was used as a negative control. NS1 interaction with liposomes was insensitive to pH over a range of 5.5 – 7.5.

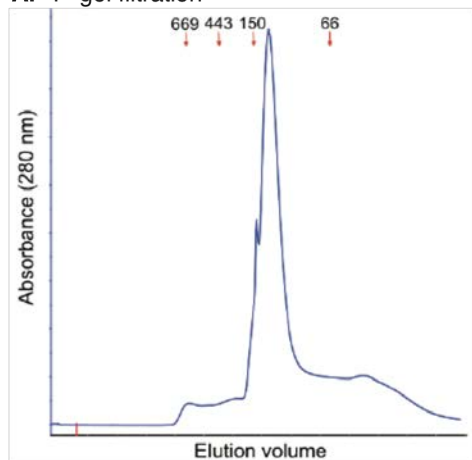
Negative-stain electron microscopy

Samples were prepared using the conventional negative staining protocol (40), and imaged at room temperature with a Morgagni 268 at 100 kV or a Tecnai T12 electron microscope (FEI Company) operated at 120 kV. For single particle analysis, images were recorded with the T12 at a magnification of 71,139x and a defocus value of ~1.6 μm on a Gatan US4000 CCD camera. All images were binned (2 x 2 pixels) to obtain a pixel size of 4.16 Å at the specimen level. A total of 7297 projections of TEV-cleaved NS1 were manually excised using Boxer [part of the EMAN 1.9 software suite].(41) Reference-free alignment and classifications into 100 classes for each sample were performed in EMAN 1.9 using refine2d.py (40, 41).

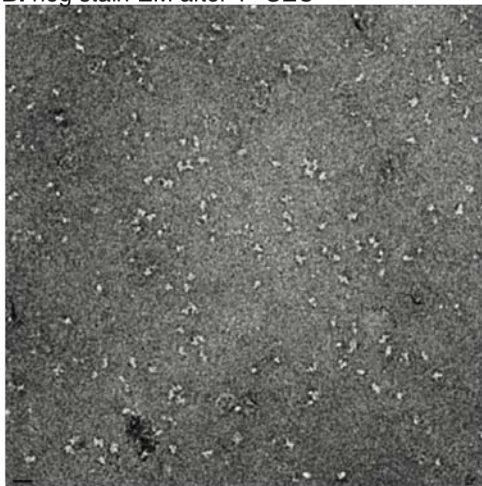
Mutagenesis in DEN2 NS1

Mutations were introduced into the DEN2 16681 infectious cDNA clone (pD2/IC-30P) (30) by standard overlapping PCR and ligated into the SphI and KasI restriction sites of pD2/IC-30P. Constructs were then digested with XbaI and *in vitro* transcribed using T7 RNA polymerase. Transcripts (10 μg) for wild type DEN2 and each of the four full-length clones containing mutations were electroporated into 1×10^7 BHK-15 cells. Supernatants collected 96-hr post-electroporation were used for plaque assays with neutral red staining after 7 days (Table S2). Plaques were visible only for the wild type (3-mm diameter) and the F160A mutant (1-mm diameter). An immunofocus virus titer assay using supernatants 96-hr post-electroporation was consistent with the plaque assay (Table S2). In a separate experiment (Fig. S6), BHK-15 cells were fixed 48 hr post electroporation using 3.7% paraformaldehyde and permeabilized using 0.1% Triton X-100 for immunofluorescence analysis with mouse monoclonal antibodies to double-stranded RNA, DEN2 envelope protein, DEN2 NS1 and DEN2 NS5 (RNA-dependent RNA polymerase). The secondary antibody was tetramethylrhodamine (TRITC)-conjugated goat anti-mouse and the nuclei were stained with Hoechst stain.

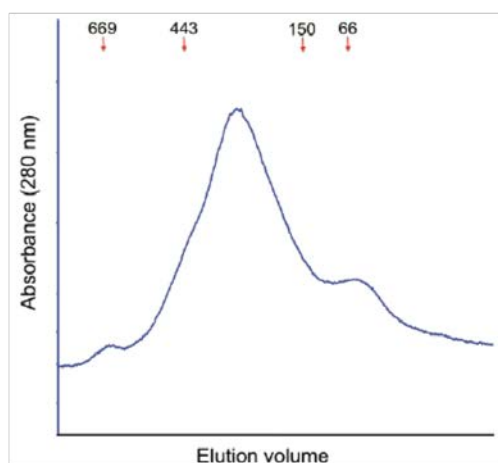
A. 1st gel filtration



B. neg stain EM after 1st SEC



C. 2nd gel filtration



D. neg stain EM after 2nd SEC

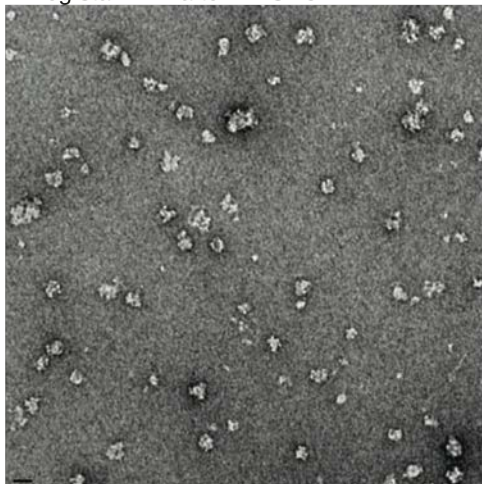


Fig. S1. Preparation of recombinant NS1. (A) Gel filtration of DEN2 NS1 following Ni-affinity purification in the presence of detergent and cleavage of the His₆ tag. No detergent was present in the elution buffer for the S200 preparative-scale column. Elution positions of molecular weight standards are indicated with arrows. (B) Negative-stain EM image of the peak fraction from the elution in A. Scale bar in the lower left is 20 nm. (C) Second detergent-free gel filtration of DEN2 NS1. Fractions from the major peak in A were pooled and eluted from a second analytical-scale S200 gel filtration column. Oligomer formation is evident from the apparent molecular weight of the peak fractions, approximately 300 kDa, corresponding to an NS1 hexamer. (D) Negative-stain EM image of the peak fraction from the elution in C, showing larger particles than in seen in B. Scale bar in the lower left is 20 nm.

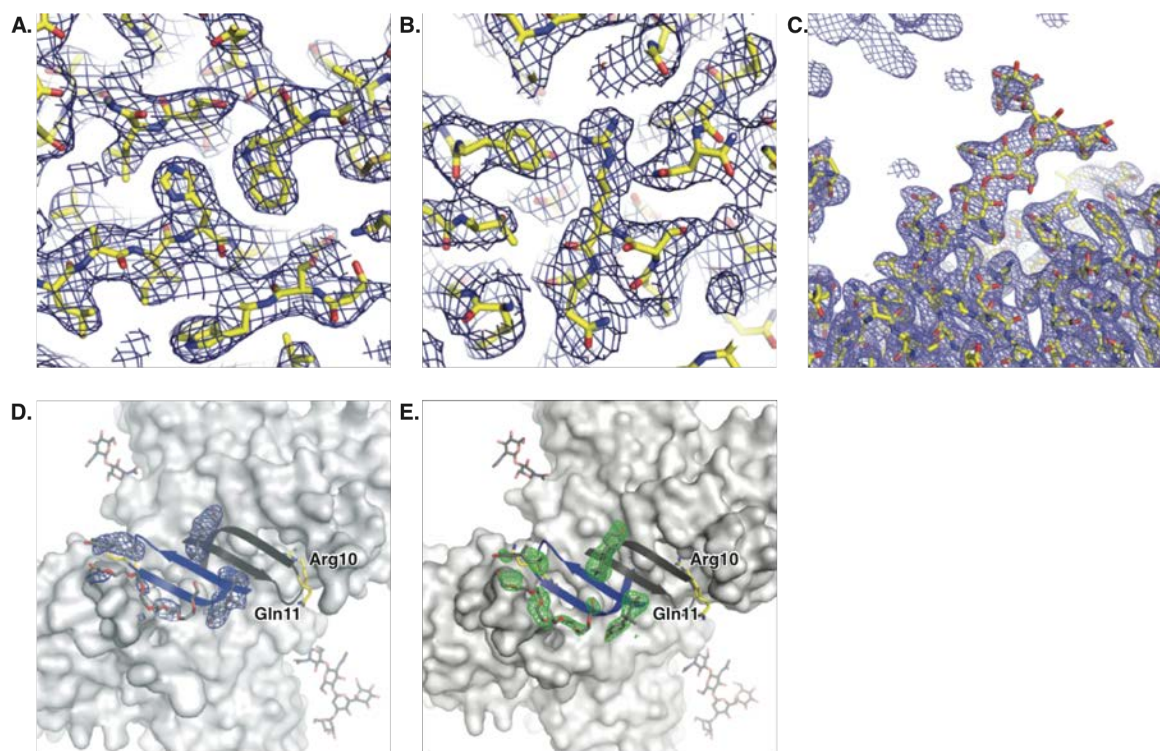


Fig. S2. Electron densities from WNV NS1 crystal form 1. (A, B) Two regions of density in the 3.0-Å map (1 σ contour) computed with phases from S-SAD followed by density modification phase refinement and extension from 4.5 Å to 3.0 Å. The starting structure was built into this map, *i.e.* the map includes NO phase information from the model. The final refined model is superimposed to illustrate the map quality. (C) Density for the carbohydrate at Asn207 in the final 2.6-Å map (2mFo-DFc, 1 σ contour). Protein and carbohydrate are shown as sticks with yellow C. (D) Density in the original 3.0-Å map shown in A and B (1 σ contour) for detergent fragments (Triton X-100 head groups and tail) bound to the hydrophobic protrusion. The final model is superimposed. (E) Omit density (Fo-Fc, 3 σ contour) for bound detergent fragments in the final 2.6-Å map. The topology of the β -roll fold is shown in the ribbon drawing with the remainder of NS1 as a gray surface. Side chains of the dipeptide implicated in NS4B interaction Arg10-Gln11 (DEN2 NS1 Asn10-Lys11), located in the β -roll loop, are shown in stick form with yellow C. Carbohydrate modification at Asn207 has black C.

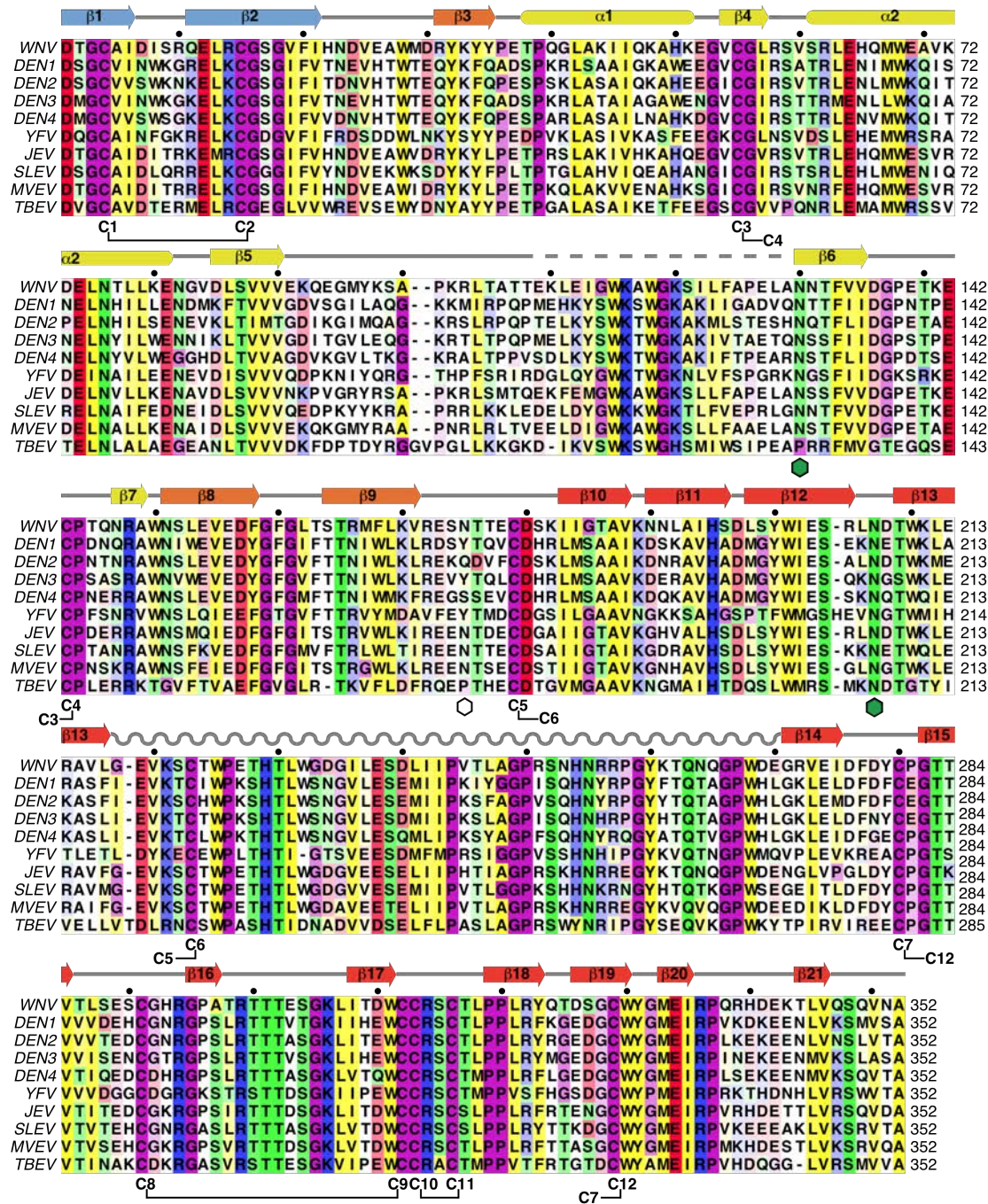


Fig. S3. Secondary structure and sequence alignment of flavivirus NS1 proteins. Secondary structure elements are colored as in Fig 1B. Conserved cysteines and disulfides are indicated under the sequences. Glycosylation sites are indicated with hexagons (green = most conserved). Accession codes: West Nile strain NY99 (WNV), ABA62343; dengue 1 strain 16007 (DEN1), AAF59976; dengue 2 strain Thailand/16681/84 (DEN2), AAB58782; dengue 3 isolate BR/D3LIMHO/2006 (DEN3), AEV42062; dengue 4 strain 814669 (DEN4), AAK01233; Japanese encephalitis strain K94P05 (JEV), AAC02714; St. Louis encephalitis strain MS1-7 (SLEV), P09732; yellow fever 17D vaccine strain (YFV), CAA27332; Murray Valley encephalitis (MVEV), NP_051124; tick-borne encephalitis (TBEV), NP_043135.

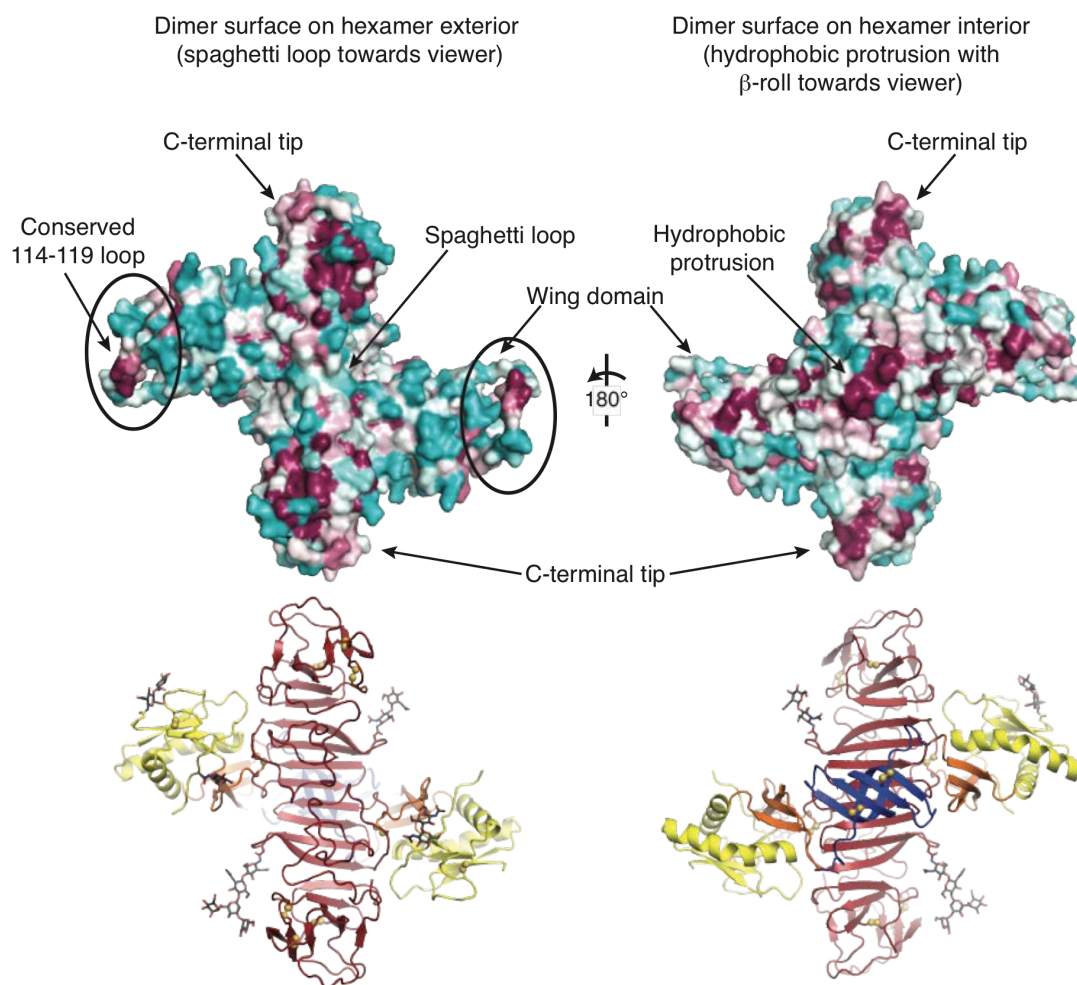


Fig. S4. NS1 sequence conservation mapped onto the protein surface. The NS1 surface is colored in a ramp (CONSUF) (42) according to sequence conservation from the most conserved (dark magenta) to the most divergent (dark cyan) based on an alignment (Clustal) (43) of NS1 sequences from 61 flaviviruses. The most conserved surfaces are on the hydrophobic protrusion which is directed towards the center of the hexamer, the C-terminal tip of the central β -ladder, and the highly flexible loop in the wing domain (amino acids 114-119, lacking density in the crystal structures, but modeled here to show the loop position and circled). Ribbon diagrams of the NS1 dimer viewed from the hexamer-external surface (lower left) and hexamer-internal surface (lower right) are included for clarity and colored as in Fig. 1.

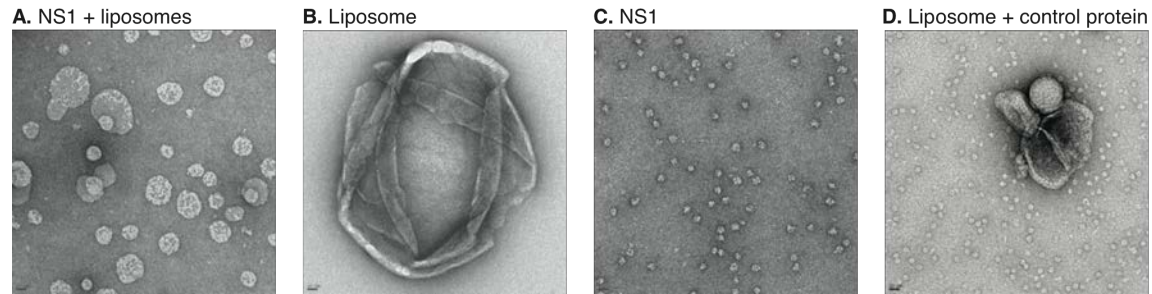


Fig. S5. NS1 remodeling of liposomes visualized by negative-stain EM. (A) Nano-particles resulting from WNV NS1 treatment of liposomes (composition 1:9 cholesterol:phosphatidylcholine) at pH 5.5 in a ratio of 585 lipid/cholesterol molecules per NS1 hexamer. All NS1 is associated with small particles and none remains in the background. (B) Untreated liposomes. (C) WNV NS1 without liposomes. (D) Liposomes treated with a control protein (MycE tetramer (39)) of similar molecular weight and isoelectric point to NS1. All images are on the same scale (scale bar 20 nm).

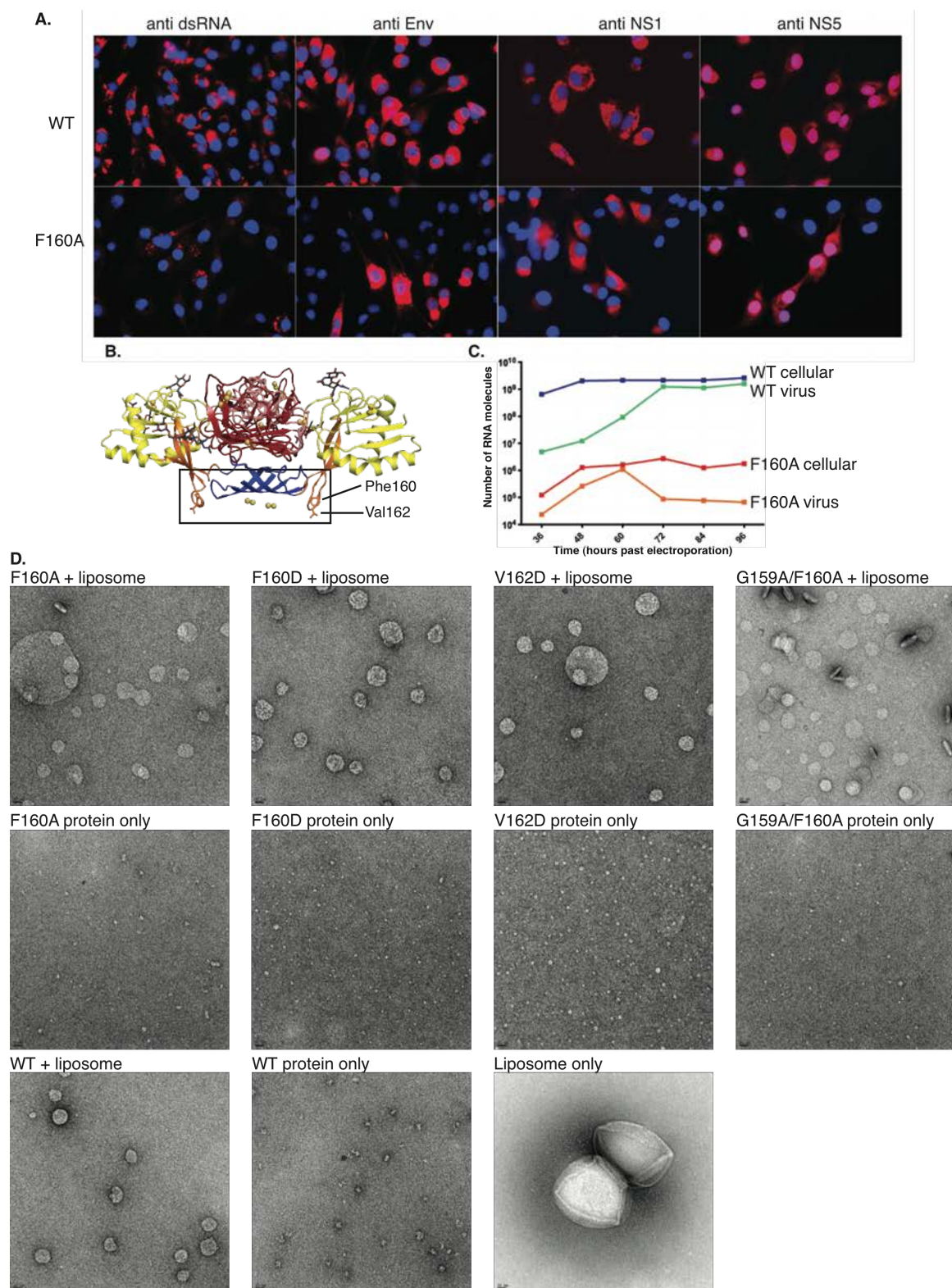


Fig. S6. DEN2 NS1 mutagenesis. NS1 mutagenesis. (A) Localization of dsRNA, E, NS1 and NS5 by immunofluorescence (IF) assay. BHK-15 cells were transfected by electroporation with

wild-type (top row) or the F160A mutant (bottom row) *in vitro* transcribed RNA. Cells were fixed at 48 hr post electroporation and subjected to IF analysis using primary monoclonal antibodies against double stranded RNA (dsRNA), E protein (ENV), NS1, or NS5, and secondary antibody TRITC-conjugated goat anti-mouse secondary antibody (red). Nuclei were stained with Hoechst stain (blue). The merged images indicate that the viral proteins and replication complexes localize similarly in the F160A mutant and in the wild-type virus. **(B)** Molecular drawing (same view as Fig. 1C) shows the position of Phe160 and Val162 in the “greasy finger” of the connector sub-domain. No plaques were recovered from the F160D, V162D, or GF159/160AA mutants (Table S2). **(C)** Total viral RNA in both virus particles and infected cells is reduced in the F160A mutant. RNA was quantitated by qRT-PCR for both the supernatant (viral particles) and lysate (infected cells) fractions from cells electroporated with either wild type or F160A *in vitro* transcribed RNA. Orange: F160A virus particles, Red: F160A cellular RNA, Green: wild type virus particles, Blue: wild type cellular RNA. **(D)** Effect of amino acid substitutions on NS1 association with liposomes. Purified wild type DEN2 NS1 and variants were incubated 2 hr at 37° C with or without liposomes in a pH 7.5 buffer and imaged by negative-stain EM, as described in Materials and Methods.

Table S1. Crystallographic Data and Refinement Statistics

	WNV form 1		WNV form 2	DEN2
	S anomalous	Native	Native	Native
Data				
Space group	<i>P</i> 321	<i>P</i> 321	<i>P</i> 3	<i>H</i> 3
Unit cell a=b, c (Å)	167.80, 93.82	168.69, 92.89	186.89, 81.77	176.34, 81.94
Wavelength (Å)	1.7462	1.0332	1.0332	0.97934
d _{min} (Å)	3.00 (3.16-3.00) ¹	2.59 (2.68-2.59)	2.75 (2.80-2.75)	3.00 (3.18-3.00)
Observations (#)	5,732,471 (667,694)	857,143 (28,659)	489,465 (26,765)	35,174 (5,648)
Unique reflections	61,538 (8,844) ²	47,162 (4,377)	82,996 (4,565)	17,731 (2,893)
Avg I/σ _I	27.8 (2.5) ²	21.1 (1.2)	7.4 (1.0)	8.8 (1.3)
R _{merge}	0.292 (4.187) ²	0.091 (1.558)	0.244 (2.410)	0.070 (0.613)
CC _{1/2} ³	0.999 (0.442) ²	0.999 (0.531)	0.992 (0.457)	0.996 (0.444)
CC* ⁴	1.000 (0.771) ²	1.000 (0.833)	0.998 (0.792)	0.999 (0.784)
Completeness %	100.0 (100.0) ²	99.5 (94.8)	100.0 (1000)	94.3 (95.1)
Wilson B (Å ²)	88.2	83.4	67.8	73.7
Refinement				
Reflections (#)		46,980	82,941	17,724
R _{work}		0.172 (0.377)	0.195 (0.341)	0.185 (0.314)
R _{free}		0.199 (0.455)	0.235 (0.316)	0.218 (0.318)
RMSD bonds (Å)		0.008	0.004	0.004
RMSD angles (°)		1.115	0.820	0.712
Atoms (#)				
Protein		5351	15996	5098
Solvent		218	15 (SO ₄ ⁻²)	0
Carbohydrate/Det		229	84	28
Avg B-factors (Å ²)				
Protein		85.0	82.8	88.6
Solvent		77.3	94.9	
Carbohydrate/Det		126.4	101.2	67.3
Ramachandran				
Favored (%)		94.8	96.4	94.7
Allowed (%)		5.2	3.3	5.3
Outliers (%)		0	0.3	0

¹Numbers in parentheses refer to the outermost shell of data.

²Anomalous pairs are treated separately.

³CC_{1/2} is the correlation of one-half of the observations with the other half (29, 30).

$$^4 CC^* = \sqrt{\frac{2CC_{1/2}}{1+CC_{1/2}}} \quad (29, 30)$$

Table S2. Phenotypic Characteristics of DEN2 NS1 Mutations

Virus	Plaque size	Titer (PFU¹/mL)
Wild type	3 mm	4.8x10 ⁶
F160A	1 mm	6.0x10 ³
F160D	Not recovered	—
G159A/F160A	Not recovered	—
V162D	Not recovered	—

¹PFU = plaque-forming units

References

1. B. D. Lindenbach, C. M. Rice, Molecular biology of flaviviruses. *Adv Virus Res* **59**, 23-61 (2003).
2. M. S. Suthar, M. S. Diamond, M. Gale, Jr., West Nile virus infection and immunity. *Nat Rev Microbiol* **11**, 115-128 (2013).
3. D. A. Muller, P. R. Young, The flavivirus NS1 protein: molecular and structural biology, immunology, role in pathogenesis and application as a diagnostic biomarker. *Antiviral Res* **98**, 192-208 (2013).
4. A. A. Khromykh, P. L. Sedlak, E. G. Westaway, cis- and trans-acting elements in flavivirus RNA replication. *J Virol* **74**, 3253-3263 (2000).
5. B. D. Lindenbach, C. M. Rice, Genetic interaction of flavivirus nonstructural proteins NS1 and NS4A as a determinant of replicase function. *J Virol* **73**, 4611-4621 (1999).
6. E. G. Westaway, J. M. Mackenzie, M. T. Kenney, M. K. Jones, A. A. Khromykh, Ultrastructure of Kunjin virus-infected cells: colocalization of NS1 and NS3 with double-stranded RNA, and of NS2B with NS3, in virus-induced membrane structures. *J Virol* **71**, 6650-6661 (1997).
7. B. D. Lindenbach, C. M. Rice, trans-Complementation of yellow fever virus NS1 reveals a role in early RNA replication. *J Virol* **71**, 9608-9617 (1997).
8. J. M. Mackenzie, M. K. Jones, P. R. Young, Immunolocalization of the dengue virus nonstructural glycoprotein NS1 suggests a role in viral RNA replication. *Virology* **220**, 232-240 (1996).
9. S. Youn *et al.*, Evidence for a genetic and physical interaction between nonstructural proteins NS1 and NS4B that modulates replication of West Nile virus. *J Virol* **86**, 7360-7371 (2012).
10. I. Gutsche *et al.*, Secreted dengue virus nonstructural protein NS1 is an atypical barrel-shaped high-density lipoprotein. *Proc Natl Acad Sci U S A* **108**, 8003-8008 (2011).
11. D. A. Muller *et al.*, Structure of the dengue virus glycoprotein non-structural protein 1 by electron microscopy and single-particle analysis. *J Gen Virol* **93**, 771-779 (2012).
12. P. Avirutnan *et al.*, Binding of flavivirus nonstructural protein NS1 to C4b binding protein modulates complement activation. *J Immunol* **187**, 424-433 (2011).
13. P. Avirutnan *et al.*, Antagonism of the complement component C4 by flavivirus nonstructural protein NS1. *J Exp Med* **207**, 793-806 (2010).
14. K. M. Chung *et al.*, West Nile virus nonstructural protein NS1 inhibits complement activation by binding the regulatory protein factor H. *Proc Natl Acad Sci U S A* **103**, 19111-19116 (2006).
15. V. D. Krishna, M. Rangappa, V. Satchidanandam, Virus-specific cytolytic antibodies to nonstructural protein 1 of Japanese encephalitis virus effect reduction of virus output from infected cells. *J Virol* **83**, 4766-4777 (2009).
16. P. R. Young, P. A. Hilditch, C. Bletchly, W. Halloran, An antigen capture enzyme-linked immunosorbent assay reveals high levels of the dengue virus protein NS1 in the sera of infected patients. *J Clin Microbiol* **38**, 1053-1057 (2000).
17. S. Alcon-LePoder *et al.*, Secretion of flaviviral non-structural protein NS1: from diagnosis to pathogenesis. *Novartis Found Symp* **277**, 233-247; discussion 247-253 (2006).
18. R. Vita *et al.*, The immune epitope database 2.0. *Nucleic Acids Res* **38**, D854-862 (2010).

19. H. J. Cheng *et al.*, Proteomic analysis of endothelial cell autoantigens recognized by anti-dengue virus nonstructural protein 1 antibodies. *Exp Biol Med (Maywood)* **234**, 63-73 (2009).
20. A. K. Falconar, The dengue virus nonstructural-1 protein (NS1) generates antibodies to common epitopes on human blood clotting, integrin/adhesin proteins and binds to human endothelial cells: potential implications in haemorrhagic fever pathogenesis. *Arch Virol* **142**, 897-916 (1997).
21. A. K. Falconar, Monoclonal antibodies that bind to common epitopes on the dengue virus type 2 nonstructural-1 and envelope glycoproteins display weak neutralizing activity and differentiated responses to virulent strains: implications for pathogenesis and vaccines. *Clin Vaccine Immunol* **15**, 549-561 (2008).
22. E. A. Henchal, L. S. Henchal, J. J. Schlesinger, Synergistic interactions of anti-NS1 monoclonal antibodies protect passively immunized mice from lethal challenge with dengue 2 virus. *J Gen Virol* **69** (Pt 8), 2101-2107 (1988).
23. I. J. Liu, C. Y. Chiu, Y. C. Chen, H. C. Wu, Molecular mimicry of human endothelial cell antigen by autoantibodies to nonstructural protein 1 of dengue virus. *J Biol Chem* **286**, 9726-9736 (2011).
24. J. R. Wilson, P. F. de Sessions, M. A. Leon, F. Scholle, West Nile virus nonstructural protein 1 inhibits TLR3 signal transduction. *J Virol* **82**, 8262-8271 (2008).
25. F. Civril *et al.*, The RIG-I ATPase domain structure reveals insights into ATP-dependent antiviral signalling. *EMBO Rep* **12**, 1127-1134 (2011).
26. C. Motz *et al.*, Paramyxovirus V proteins disrupt the fold of the RNA sensor MDA5 to inhibit antiviral signaling. *Science* **339**, 690-693 (2013).
27. W. C. Brown *et al.*, New ligation-independent cloning vectors compatible with a high-throughput platform for parallel construct expression evaluation using baculovirus-infected insect cells. *Protein Expr Purif* **77**, 34-45 (2011).
28. W. Kabsch, XDS. *Acta Crystallogr D Biol Crystallogr* **66**, 125-132 (2010).
29. P. A. Karplus, K. Diederichs, Linking crystallographic model and data quality. *Science* **336**, 1030-1033 (2012).
30. K. Diederichs, P. A. Karplus, Better models by discarding data? *Acta Crystallogr D Biol Crystallogr* **69**, 1215-1222 (2013).
31. G. M. Sheldrick, Experimental phasing with SHELXC/D/E: combining chain tracing with density modification. *Acta Crystallogr D Biol Crystallogr* **66**, 479-485 (2010).
32. CCP4, The CCP4 Suite: Programs for Protein Crystallography. *Acta Cryst.* **D**, 760-763 (1994).
33. K. Cowtan, The Buccaneer software for automated model building. 1. Tracing protein chains. *Acta Crystallogr D Biol Crystallogr* **62**, 1002-1011 (2006).
34. P. Emsley, K. Cowtan, Coot: model-building tools for molecular graphics. *Acta Crystallogr D Biol Crystallogr* **60**, 2126-2132 (2004).
35. G. N. Murshudov, A. A. Vagin, E. J. Dodson, Refinement of macromolecular structures by the maximum-likelihood method. *Acta Crystallogr D Biol Crystallogr* **53**, 240-255 (1997).
36. P. D. Adams *et al.*, PHENIX: building new software for automated crystallographic structure determination. *Acta Crystallogr D Biol Crystallogr* **58**, 1948-1954 (2002).
37. V. B. Chen *et al.*, MolProbity: all-atom structure validation for macromolecular crystallography. *Acta Crystallogr D Biol Crystallogr* **66**, 12-21 (2010).

- 38. E. Krissinel, K. Henrick, Inference of macromolecular assemblies from crystalline state. *J Mol Biol* **372**, 774-797 (2007).
- 39. D. L. Akey *et al.*, A new structural form in the SAM/metal-dependent omethyltransferase family: MycE from the mycinamicin biosynthetic pathway. *J Mol Biol* **413**, 438-450 (2011).
- 40. M. Ohi, Y. Li, Y. Cheng, T. Walz, Negative Staining and Image Classification - Powerful Tools in Modern Electron Microscopy. *Biol Proced Online* **6**, 23-34 (2004).
- 41. S. J. Ludtke, P. R. Baldwin, W. Chiu, EMAN: semiautomated software for high-resolution single-particle reconstructions. *J Struct Biol* **128**, 82-97 (1999).
- 42. H. Ashkenazy, E. Erez, E. Martz, T. Pupko, N. Ben-Tal, ConSurf 2010: calculating evolutionary conservation in sequence and structure of proteins and nucleic acids. *Nucleic Acids Res* **38**, W529-533 (2010).
- 43. M. A. Larkin *et al.*, Clustal W and Clustal X version 2.0. *Bioinformatics* **23**, 2947-2948 (2007).